This article has been accepted for publication in a future issue of this journal, but has not been fully edited. Content may change prior to final publication. Citation information: DOI 10.1109/TIE.2021.3097612, IEEE Transactions on Industrial Electronics

Three-Winding-Coupled-Inductor-Based Dual Active Bridge DC-DC Converter with Full Load Range ZVS Under Wide Voltage Range

Hua Han, *Member, IEEE*, Jing Guo, *Student Member*, Guo Xu, *Senior Member*, *IEEE*, Jingtao Xu, Dong Liu, *Senior Member*, *IEEE*, and Mei Su, *Member*, *IEEE*

***Abstract*—In this paper, a three-winding-coupled -inductor-based dual active bridge (TWCI DAB) DC-DC converter is proposed. Similar to the current-fed DAB converter, the proposed TWCI DAB has small input current ripple and wide input voltage range. In addition, the zero-voltage-switching (ZVS) of all switches in the full load range under wide input voltage variation can be realized. With the magnetic integration structure, the size of the total magnetics can be reduced, and the efficiency is also increased compared with the discrete magnetic case. To better analyze the working principle of the three-winding -coupled-inductor, a general analysis method based on magnetic reluctance model is firstly introduced to obtain the expressions of high frequency current. Furthermore, ZVS analysis and inductor design to obtain low inductor root mean square (RMS) current and full load range ZVS based on the ZVS conditions, maximum power transfer and RMS current are presented. Finally, the validity of the proposed topology and design are verified by experimental results from a 1-kW laboratory prototype.**

***Index Terms*—Dual active bridge, three-winding-coupled -inductor, wide voltage gain range, zero voltage switching.**

I. INTRODUCTION

Bidirectional DC-DC converters are widely used in energy storage systems, electric vehicles and distributed renewable energy power generation systems as a power link between batteries and high voltage bus [1], [2]. Although the non-isolated buck/boost converter is simple in structure [3], it is unsuitable for high voltage gain applications due to limited voltage conversion gain. Isolated bidirectional DC-DC converter with high frequency has been widely used due to its flexible voltage gain. Among them, dual active bridge (DAB) is a typical solution for bidirectional DC-DC converter [4] [5]. The topology of DAB converter mainly includes voltage-fed (VF) DAB and current-fed (CF) DAB.

For VF-DAB, in order to reduce the circulation loss, increase the voltage gain and extend the zero-voltage-switching (ZVS) range, various improvements of modulation strategies [6], [7] and topologies [8]-[10] have been proposed. However, for VF-DAB, it is difficult to achieve full load range soft-switching under wide voltage range application. Moreover, in battery charging application, during charging and discharging, voltage fluctuates in a very wide range, and the current ripple of VF-DAB port is relatively large, which may have impact on battery life [11]. For the purpose of facing with wide voltage range and reducing current fluctuations, the current-fed bidirectional DC-DC converter is an appropriate choice [12]-[18].

A current-fed bidirectional DC-DC topology with two-half-bridge using single phase shift (SPS) modulation was proposed in [13]. The low voltage side of the converter can be equivalent to the boost circuit, so it has the advantages of high voltage gain and small current ripple. However, due to the half bridge structure, the current stresses of the low voltage side switches are relatively large. The buck/boost converter and DAB converter are combined to form a staggered structure by sharing some switches to handle high current [14]. At the same time, the staggered structure of the current-fed dual active bridge (CF-DAB) DC-DC converter can significantly reduce the current ripple [15]. However, when the voltage conversion ratio changes, the circulation loss is relatively high. In order to reduce the circulation loss, a natural clamp current-fed converter is proposed to improve the topology [16]. But for low voltage side switches, ZVS may be lost. Another idea is to improve the modulation strategy, using pulse width modulation (PWM) plus phase shift control (PPS) [17], gaining low root mean square (RMS) current and wide ZVS range. In order to further reduce the circulation current, PWM plus dual phase shift (PDPS) control [18], [19] and dual PWM plus phase shift (DPPS) control [12] were proposed. Basically, these controls utilize more control degrees of freedom to obtain better performance, which makes the modulation more complex.

In CF-DAB, although the improved modulation strategies and topologies can improve the performance. However, the

Manuscript received December 18, 2020; revised April 08, 2021, June 07 2021; accepted July 01, 2021. This work was supported in part by the Nature Science Foundation of China under Grant 51907206, and 61933011, the Hunan Provincial Key Laboratory of Power Electronics Equipment and Grid under Grant 2018TP1001, and the Fundamental Research Funds in the Central South University under Grant 2021zzts0713. (Corresponding author: *Guo Xu*).

H. Han, J. Guo, G. Xu, J. Xu, and M. Su are with the School of Automation, Central South University and with Hunan Provincial Key Laboratory of Power Electronics Equipment and Grid, Changsha, 410083, China, (e-mail: hua_han@126.com; guojingcsu@csu.edu.cn; xuguocsu@csu.edu.cn; xjt4ugo@csu.edu.cn; sumeicsu@csu.edu.cn).

Dong Liu is with the Department of Electronic and Electrical Engineering, University of Sheffield, Sheffield S1 3JD, United Kingdom (e-mail: liudong@ieee.org).

0278-0046 (c) 2021 IEEE. Personal use is permitted, but republication/redistribution requires IEEE permission. See http://www.ieee.org/publications_standards/publications/rights/index.html for more information.
Authorized licensed use limited to: Central South University. Downloaded on August 12,2021 at 11:35:38 UTC from IEEE Xplore. Restrictions apply.

This article has been accepted for publication in a future issue of this journal, but has not been fully edited. Content may change prior to final publication. Citation information: DOI 10.1109/TIE.2021.3097612, IEEE Transactions on Industrial Electronics

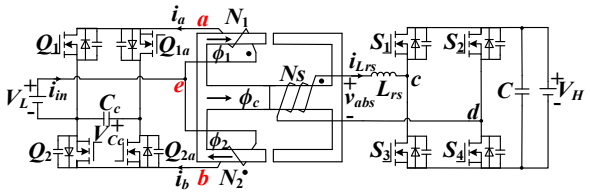

Fig.1. The topology of proposed TWCI DAB.

dual boost topology in the above-mentioned CF-DAB has two DC inductors, one leakage inductor and a transformer, which would increase the number of magnetic elements, thus increasing the occupying volume and related loss. In [20] and [21], the two DC inductors on the LVS are coupled and integrated. The power density has been improved to a certain extent. However, the design of coupled inductors is not discussed. The high voltage gain ratio can be obtained with series connection of the outputs of an interleaved bidirectional buck-boost converter and a dual-active half-bridge converter, using the windings of a coupled inductor [22]-[24]. However, the advantages of using a coupled inductor in such topologies are not clearly articulated. Adding another transformer can extend the conversion gain as well [19] by using fewer switches. In addition, coupled inductors are used in some VF-DAB literatures to reduce the number of magnetic elements and increase the power density [25]-[27]. For input-parallel-output -parallel connected DAB in [25], [26], the high-frequency link of paralleled converters is connected by a coupled inductor, which helps suppress the unbalanced current. A coupled inductor is integrated into two LVS full bridges for ZVS operation throughout full-load range [27]. However, the coupled inductors are only used to integrate the DC inductors [20], [21] or worked as transformer [19], [22]-[24] of CF-DAB or used to integrate the leakage inductors [25]-[27] of parallel VF-DAB converters. This means that magnetic integration is only applied to part of the magnetic elements in the converter. Though, the power density is improved, the overall integration of converter is still low. In order to further reduce the number of magnetic elements and improve the power density, reference can be made to other magnetic integration design methods that has been adopted to other types of converters [28]-[33].

For interleaved buck/boost converter [29] and single-phase high step-up/step-down buck/boost converter [30], coupled inductor was adopted to effectively reduce the loss of magnetic core and improve the efficiency and power density. In addition to the use of standard E magnetic cores for inductor coupling in some converters, a new structure of coupled inductor magnetic cores was studied [31], which is more uniform in magnetic flux and heat distribution as well as can improve the efficiency. For current-doubler rectifier circuit, the magnetic integration structure proposed in [32] is the earliest inductor and transformer integration. However, due to the existence of the windings of transformer secondary side, the copper loss of integrated magnetic is relatively large. On this basis, the source shifting equivalent method is used to split the secondary side windings of the transformer into two outer legs, and the shared windings with the two inductors can effectively reduce copper loss and achieve a more compact and efficient design [33].

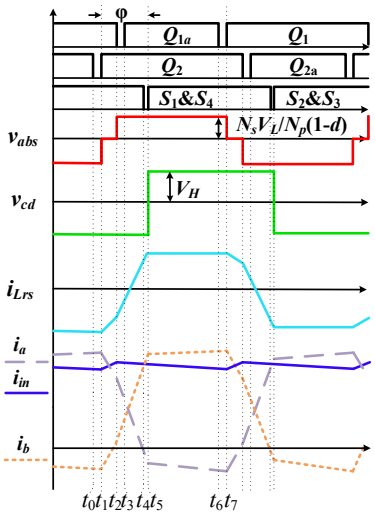

Fig.2. Steady-state waveforms for proposed TWCI DAB in boost mode. (Interval A: $\varphi \in [(2d\text{-}1)\,\pi, \pi]$).

In this paper, a new three-winding-coupled-inductor-based dual active bridge (TWCI DAB) DC-DC converter is proposed. The proposed solution has the following advantages.

a) The proposed TWCI DAB has similar performance to the CF-DAB with small input current ripple and wide voltage range. In addition, the integrated magnetic structure can significantly improve the power density and efficiency.

b) The proposed TWCI DAB can realize ZVS of all switches in the full load range under the condition of wide input voltage variation with the adopted PWM modulation. In addition, all the working modes are analyzed based on the integrated magnetic reluctance model, and a general analysis method of TWCI is provided.

c) Based on the analysis of working modes of the proposed TWCI DAB, mathematical expressions of the ZVS conditions for all switches are derived, and parameters optimization design for achieving full load range ZVS are discussed. It should be noted that, unlike the previous studies, the RMS current, ZVS ranges and maximum power transfer capability are all considered for the inductors design.

The rest of this article is organized as follows. The working principle and working modes analysis are descripted in Section II. In Section III, power characteristic and soft-switching conditions are discussed in detail. The parameters optimization design of the inductors, magnetic flux and comparative analysis of magnetics design are shown in Section IV. Section V presents the system parameters design. Section VI illustrates the experimental results to verify the effectiveness of the proposed solution. Section VII provides the conclusions.

II. Operation Principle

The topology of TWCI DAB converter is depicted in Fig.1. In the low voltage side (LVS), V_L represents the wide range voltage. C_c is the clamping capacitor. N_1 and N_2 are turns number of the two LVS windings of coupled inductors, respectively. And N_s is the turns number of high voltage side (HVS) winding. The inductor L_{rs} denotes the leakage inductor

0278-0046 (c) 2021 IEEE. Personal use is permitted, but republication/redistribution requires IEEE permission. See http://www.ieee.org/publications_standards/publications/rights/index.html for more information.
Authorized licensed use limited to: Central South University. Downloaded on August 12,2021 at 11:35:38 UTC from IEEE Xplore. Restrictions apply.

This article has been accepted for publication in a future issue of this journal, but has not been fully edited. Content may change prior to final publication. Citation information: DOI 10.1109/TIE.2021.3097612, IEEE Transactions on Industrial Electronics

on the secondary side of the TWCI. C is the HVS filter capacitor. The converter works in the boost mode as the power flows from the LVS to the HVS; otherwise, it works in the buck mode.

Fig.2 shows PWM modulation signals and the steady-state waveforms of the converter operating in boost mode. The boost mode is mainly analyzed since the working principles of the two modes are symmetrical. The duty ratio d of the switches Q_1 and Q_2 makes the voltage clamp of clamping capacitor C_c to be V_{Cc}. v_{abs} is an induced electromotive force generated by v_{ab}. S_1-S_4 are driven by pulse signals with 50% duty cycles. And the phase-shift control is applied between the LVS and the HVS.

To analyze the TWCI magnetic technique, the magnetic reluctance model of TWCI is shown in the Fig.3.

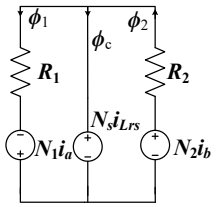

Fig.3. Magnetic reluctance model of TWCI.

The core reluctance is ignored since it is rather small compared with the air gap, R_1 and R_2 are the air gap reluctances of two outer legs respectively. In this paper, it is designed that $N_1 = N_2 = N_p$ and $R_1 = R_2 = R_p$ in order to simplify the working modes and analysis. N_p is the turns of the LVS winding, and R_p is the reluctance. According to the superposition theorem, the magnetic flux in each core leg is derived as

$$\begin{cases} \phi_1 = \dfrac{N_p i_a + N_s i_{Lrs}}{R_P} \\ \phi_c = \dfrac{-N_p (i_a - i_b) - 2N_s i_{Lrs}}{R_P} \\ \phi_2 = \dfrac{-N_s i_{Lrs} + N_p i_b}{R_P} \end{cases} \tag{1}$$

According to Faraday's law of electromagnetic induction, the voltages of the three windings can be written as

$$v_{ae} = -N_1 \frac{d\phi_1}{dt}, v_{be} = -N_2 \frac{d\phi_2}{dt}, v_{abs} = N_s \frac{d\phi_c}{dt} \tag{2}$$

At the same time, according to the relationship between the slope of the leakage inductor current and the voltage across the leakage inductor, v_{abs} can be written as

$$v_{abs} = L_{rs} \frac{di_{Lrs}}{dt} + v_{cd} \tag{3}$$

The circuit working modes are shown in Fig.4, and the detailed circuit analysis is as follows.

Stage 1 (before t_0): During this stage, Q_1, Q_{2a}, S_2 and S_3 are turned on as shown in Fig.4 (a). The N_1, N_2, N_s windings are all conducted. Consequently, v_{ae} and v_{be}, which are the voltages across N_1 and N_2 respectively, and the mid-point voltage v_{cd} of the two arms of the HVS are expressed as

$$v_{ae} = -V_L, v_{be} = V_{Cc} - V_L, v_{cd} = -V_H \tag{4}$$

Then, according to Faraday's Law, the relation between the voltages and the magnetic flux of the TWCI can be obtained as

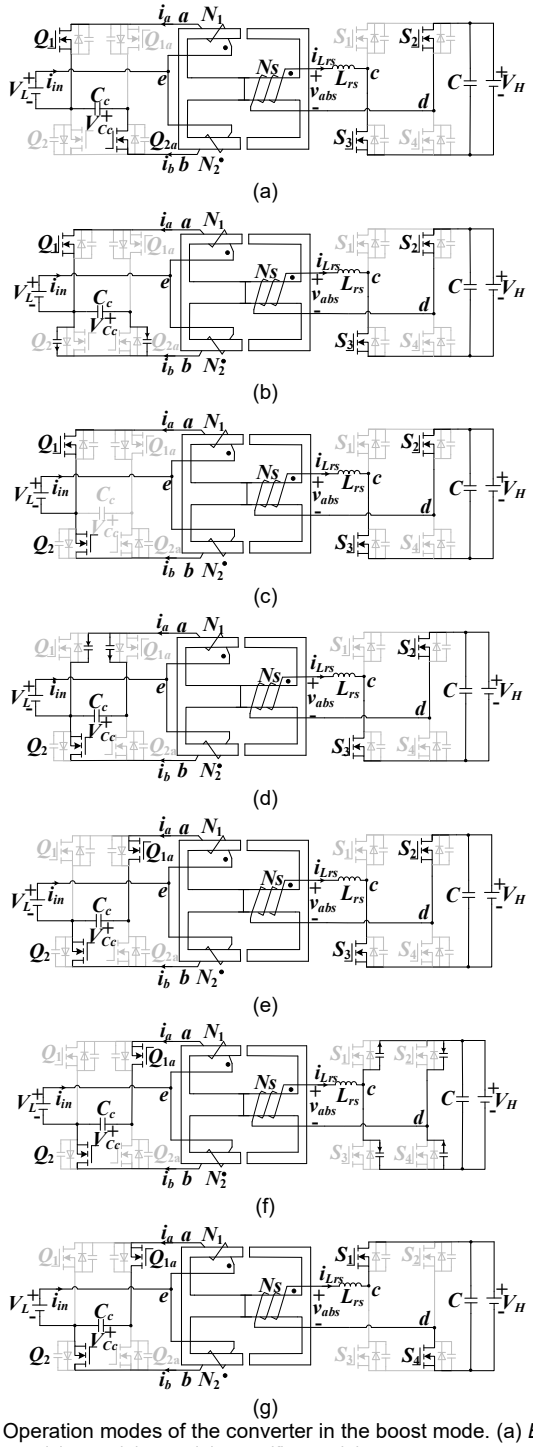

Fig.4. Operation modes of the converter in the boost mode. (a) *Before* t_0. (b) t_0-t_1. (c) t_1-t_2. (d) t_2-t_3. (e) t_3-t_4. (f) t_4-t_5. (g) t_5-t_6.

$$\begin{cases} \dfrac{d\phi_1}{dt} = \dfrac{V_L}{N_p} \\ \dfrac{d\phi_2}{dt} = \dfrac{-V_{Cc} + V_L}{N_p} \\ \dfrac{d\phi_c}{dt} = \dfrac{L_{rs}}{N_s} \dfrac{di_{Lrs}}{dt} - \dfrac{V_H}{N_s} \end{cases} \tag{5}$$

According to (1) and (5), the current slope of three windings

0278-0046 (c) 2021 IEEE. Personal use is permitted, but republication/redistribution requires IEEE permission. See http://www.ieee.org/publications_standards/publications/rights/index.html for more information.
Authorized licensed use limited to: Central South University. Downloaded on August 12,2021 at 11:35:38 UTC from IEEE Xplore. Restrictions apply.

This article has been accepted for publication in a future issue of this journal, but has not been fully edited. Content may change prior to final publication. Citation information: DOI 10.1109/TIE.2021.3097612, IEEE Transactions on Industrial Electronics

and v_{abs} can respectively be derived as

$$\begin{cases} \dfrac{di_a}{dt} = \dfrac{V_{Cc}N_s^2 - N_pN_sV_H + L_{rs}R_pV_L}{L_{rs}N_p^2} \\ \dfrac{di_{Lrs}}{dt} = \dfrac{N_pV_H - N_sV_{Cc}}{L_{rs}N_p} \\ \dfrac{di_b}{dt} = \dfrac{-V_{Cc}N_s^2 + N_pN_sV_H + L_{rs}\left(R_pV_L - R_pV_{Cc}\right)}{L_{rs}N_p^2} \\ v_{abs} = -\dfrac{N_s}{N_p}V_{Cc} \end{cases} \tag{6}$$

Stage 2 (t_0- t_1): At t_0, Q_{2a} is turned off. At this time, i_b charges C_{2a} and discharges C_2 until the body diode of Q_2 is conducted. It can be deduced that the condition for Q_2 to achieve ZVS conduction is i_b (t_0) < 0.

Stage 3 (t_1-t_2): At t_1, Q_2 is turned on under ZVS. Therefore, v_{ae}, v_{be} and v_{cd} are expressed as

$$v_{ae} = -V_L, v_{be} = -V_L, v_{cd} = -V_H \tag{7}$$

Similarly, the current slope and v_{abs} can be written as

$$\begin{cases} \dfrac{di_a}{dt} = \dfrac{-N_pN_sV_H + L_{rs}R_pV_L}{L_{rs}N_p^2} \\ \dfrac{di_{Lrs}}{dt} = \dfrac{V_H}{L_{rs}} \\ \dfrac{di_b}{dt} = \dfrac{N_pN_sV_H + L_{rs}R_pV_L}{L_{rs}N_p^2} \end{cases}, \quad v_{abs} = 0 \tag{8}$$

Stage 4 (t_2-t_3): Q_1 is turned off at t_2. i_a charges C_1 and discharges C_{1a} until the body diode of Q_{1a} is conducted. It can be deduced that the condition for Q_{1a} to achieve ZVS conduction is i_a (t_2) > 0.

Stage 5 (t_3-t_4): At t_3, Q_{1a} is turned on under ZVS. At this stage, v_{ae}, v_{be} and v_{cd} are expressed as

$$v_{ae} = V_{Cc} - V_L, v_{be} = -V_L, v_{cd} = -V_H \tag{9}$$

Likewise, the current slope and v_{abs} can be calculated as

$$\begin{cases} \dfrac{di_a}{dt} = \dfrac{-N_s^2V_{Cc} - N_pN_sV_H + L_{rs}\left(R_pV_L - R_pV_{Cc}\right)}{L_{rs}N_p^2} \\ \dfrac{di_{Lrs}}{dt} = \dfrac{N_pV_H + N_sV_{Cc}}{L_{rs}N_p} \\ \dfrac{di_b}{dt} = \dfrac{N_s^2V_{Cc} + N_pN_sV_H + L_{rs}R_pV_L}{L_{rs}N_p^2} \end{cases}, v_{abs} = \frac{N_s}{N_p}V_{Cc} \tag{10}$$

Stage 6 (t_4-t_5): At time t_4, S_2 and S_3 are turned off. The leakage inductor current charges C_{s2} and C_{s3} and discharges C_{s1} and C_{s4} until the body diodes of S_1 and S_4 are conducted. The condition for S_1 and S_4 to achieve ZVS is i_{Lrs} (t_4) > 0.

Stage 7 (t_5-t_6): At time t_5, S_1 and S_4 are turned on under ZVS. Accordingly, v_{ae}, v_{be} and v_{cd} are expressed as

$$v_{ae} = V_{Cc} - V_L, v_{be} = -V_L, v_{cd} = V_H \tag{11}$$

Correspondingly, the current slope and v_{abs} can be written as (12).

$$\begin{cases} \dfrac{di_a}{dt} = \dfrac{-N_s^2V_{Cc} + N_pN_sV_H + L_{rs}\left(R_pV_L - R_pV_{Cc}\right)}{L_{rs}N_p^2} \\ \dfrac{di_{Lrs}}{dt} = \dfrac{-N_pV_H + N_sV_{Cc}}{L_{rs}N_p} \\ \dfrac{di_b}{dt} = \dfrac{N_s^2V_{Cc} - N_pN_sV_H + L_{rs}R_pV_L}{L_{rs}N_p^2} \\ v_{abs} = \dfrac{N_s}{N_p}V_{Cc} \end{cases} \tag{12}$$

The previous analysis provides a general analysis method of TWCI based on magnetic reluctance model. The current slope in each mode can be obtained, which is an important basis for analysis of power characteristics and ZVS.

III. Power Characteristics and ZVS Analysis

A、 Transmission Power with PPS Control

As Fig.2 shown, the phase shift angle between the rising edge of v_{abs} and v_{cd} is defined as φ. The total volt-seconds applied to the N_1 or N_2 winding of LVS over one switching period are

$$-V_Ld + \left(-V_L + V_{Cc}\right)\left(1-d\right) = 0 \tag{13}$$

Consequently, the duty cycle of Q_1 and Q_2 is given by

$$d = 1 - \frac{V_L}{V_{Cc}} \tag{14}$$

where V_{Cc} is the voltage across the clamping capacitor C_c and is a fixed value.

V_{Cc} is controlled to match the output voltage, and current slope of leakage inductor is zero during the power transmission stage 1 and 7. The turns number relationship of the TWCI can be obtained as

$$\frac{N_p}{N_s} = \frac{V_{Cc}}{V_H} \tag{15}$$

Through integration of the transformer voltage and current under PPS control, the power can be calculated as

$$P = \begin{cases} \dfrac{V_H^2\left(1-d\right)\left[\varphi - \left(d-0.5\right)\pi\right]T_s}{\pi L_{rs}} & \varphi \subset \left[0, \left(2d-1\right)\pi\right] \\ \dfrac{V_H^2\left[-\varphi^2 + 2d\pi\varphi - d\left(2d-1\right)\pi^2\right]T_s}{2\pi^2L_{rs}} & \varphi \subset \left[\left(2d-1\right)\pi, \pi\right] \end{cases} \tag{16}$$

Fig.5 illustrates the relationship between transmission power

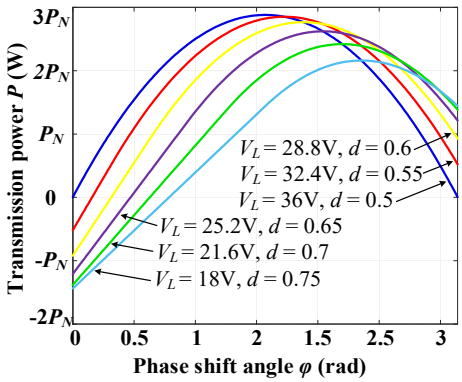

Fig.5. Curves of transmission power and phase shift angle.

0278-0046 (c) 2021 IEEE. Personal use is permitted, but republication/redistribution requires IEEE permission. See http://www.ieee.org/publications_standards/publications/rights/index.html for more information.
Authorized licensed use limited to: Central South University. Downloaded on August 12,2021 at 11:35:38 UTC from IEEE Xplore. Restrictions apply.

This article has been accepted for publication in a future issue of this journal, but has not been fully edited. Content may change prior to final publication. Citation information: DOI 10.1109/TIE.2021.3097612, IEEE Transactions on Industrial Electronics

and phase shift angle under PPS control. Under different voltages V_L, when the voltage matches and the phase shift angle φ range is [0, 0.5π], the transmission power increases monotonically as the phase shift angle increases.

B、 ZVS Range Analysis

Based on mode analysis and calculation of instantaneous current, the current limit for charging/discharging the junction capacitor C_{2a}/C_2 to achieve ZVS of Q_1 and Q_2 is written as

$$I_{ZVS\_Q_1\&Q_2} = i_b(t_0) = \begin{cases} \dfrac{R_p T_s (V_L - V_{Cc}) V_L}{2N_p^2 V_{Cc}} & \dfrac{\varphi}{\pi} \subset [0,(2d-1)] \\ \dfrac{P}{2V_L} + \dfrac{R_p T_s V_L^2}{2N_p^2 V_{Cc}} - \dfrac{R_p T_s V_L}{2N_p^2} - \dfrac{V_H^2 T_s}{4V_{Cc} L_{rs}} + \dfrac{V_H}{2V_{Cc} L_{rs}} \sqrt{\dfrac{V_H^2 T_s^2 V_L}{V_{Cc}} \left(1 - \dfrac{V_L}{V_{Cc}}\right) - 2L_{rs} T_s P} & \dfrac{\varphi}{\pi} \subset [(2d-1),1] \end{cases} \tag{17}$$

The current limit for charging/discharging the junction capacitor C_{1a}/C_1 to achieve ZVS of Q_{1a} and Q_{2a} can be obtained in the same way, which is written as

$$I_{ZVS\_Q_{1a}\&Q_{2a}} = i_a(t_2) = \begin{cases} -\dfrac{R_p T_s (V_L - V_{Cc}) V_L}{2N_p^2 V_{Cc}} & \dfrac{\varphi}{\pi} \subset [0,(2d-1)] \\ \dfrac{P}{2V_L} - \dfrac{R_p T_s V_L^2}{2N_p^2 V_{Cc}} + \dfrac{R_p T_s V_L}{2N_p^2} - \dfrac{V_H^2 T_s}{4V_{Cc} L_{rs}} + \dfrac{V_H^2 T_s V_L}{V_{Cc}^2 L_{rs}} - \dfrac{V_H}{2V_{Cc} L_{rs}} \sqrt{\dfrac{V_H^2 T_s^2 V_L}{V_{Cc}} \left(1 - \dfrac{V_L}{V_{Cc}}\right) - 2L_{rs} T_s P} & \dfrac{\varphi}{\pi} \subset [(2d-1),1] \end{cases} \tag{18}$$

And the ZVS current limit for charging/discharging the junction capacitor of all the HVS switches is written as

$$I_{ZVS\_S_1\&S_2\&S_3\&S_4} = i_{Lrs}(t_4) = \begin{cases} \dfrac{V_H T_s (V_{Cc} - 2V_L)}{4V_{Cc} L_{rs}} & \dfrac{\varphi}{\pi} \subset [0,(2d-1)] \\ \dfrac{V_H T_s}{4L_{rs}} - \dfrac{1}{2L_{rs}} \sqrt{\dfrac{V_H^2 T_s^2 V_L}{V_{Cc}} \left(1 - \dfrac{V_L}{V_{Cc}}\right) - 2L_{rs} T_s P} & \dfrac{\varphi}{\pi} \subset [(2d-1),1] \end{cases} \tag{19}$$

From (17) - (19) of the ZVS analysis above, it can be seen that after the specification parameters are determined, such as transmission power and winding turns ratio, etc., the ZVS of the converter switches are only related to N_p^2/R_p and leakage inductor L_{rs}. To make the expression simple, it is defined that $L_{eq} = N_p^2/R_p$.

IV. Design Considerations

A、 ZVS Design Related to L_{eq} and Leakage Inductor

In this section, the parameter considerations for L_{eq} and leakage inductor L_{rs} are discussed with the goal of achieving full load range ZVS. The related parameters are: V_L = 18~36V, V_H = 360V, P_N = 1kW. According to (14), the duty cycle range is 0.5~0.75.

According to the ZVS current limit formula of each switch,

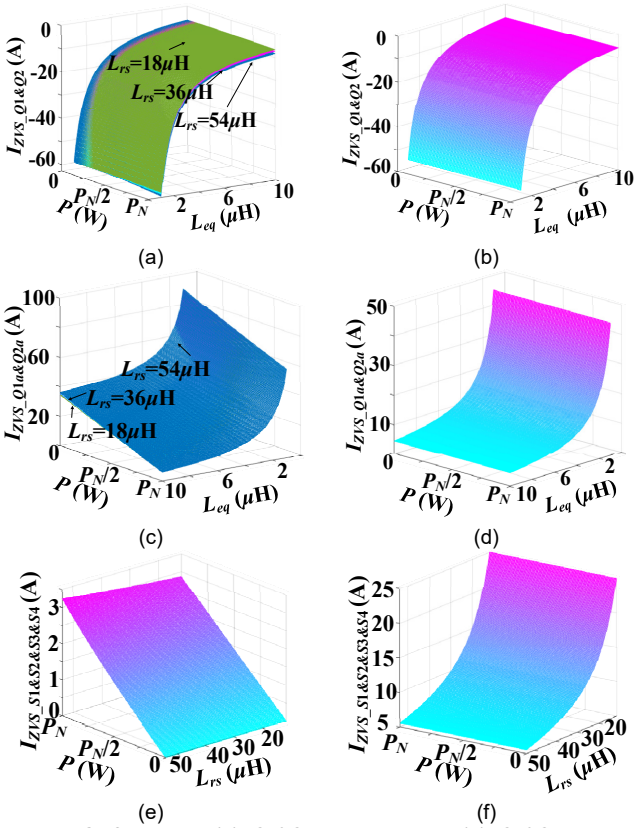

Fig.6. ZVS of switches. (a): Q_1&Q_2 when V_L = 36V. (b): Q_1&Q_2 when V_L = 18V. (c): Q_{1a}&Q_{2a} when V_L = 36V. (d): Q_{1a}&Q_{2a} when V_L = 18V. (e): S_1&S_2&S_3&S_4 when V_L = 36V. (f): S_1&S_2&S_3&S_4 when V_L = 18V. (V_L = 18~36V, V_H = 360V, P_N = 1kW).

Fig.6 (a) and (b) show ZVS of the LVS switches Q_1 and Q_2 at different d. When d is equal to 0.5, from no load to the rated power point P_N, the current is less than zero; when d is equal to 0.75, the current is less than zero from no load to P_N. Consequently, despite the change in d and leakage inductor value L_{rs}, within the range of [2μH, 10μH] for the equivalent inductors L_{eq} of outer legs, the current value $I_{ZVS\_Q1\&Q2}$ is always less than zero. It means that the ZVS of the LVS switches Q_1 and Q_2 can be achieved in the full load range with different L_{eq}. Similarly, Fig.6 (c), (d), (e) and (f) show that ZVS of other switches can also be realized within the full load range. Therefore, the appropriate value range of L_{eq} and leakage inductor L_{rs} can be preliminarily selected by ZVS design. However, the inductor RMS current should also be considered to achieve a smaller inductor loss.

B、 Inductor RMS Current Design Considerations

In this section, the design considerations for leakage inductor L_{rs} and L_{eq} are discussed with the goal of obtaining low RMS current.

For the leakage inductor design, from the relationship between the transmission power and the phase shift angle φ in Fig.4, when the phase shift angle φ = 0.5π, the relationship between the transmission power versus the leakage inductor L_{rs} and the duty cycle is written as (20).

Fig.7 shows that the corresponding leakage inductor is different under different d when the rated power is transmitted.

0278-0046 (c) 2021 IEEE. Personal use is permitted, but republication/redistribution requires IEEE permission. See http://www.ieee.org/publications_standards/publications/rights/index.html for more information.
Authorized licensed use limited to: Central South University. Downloaded on August 12,2021 at 11:35:38 UTC from IEEE Xplore. Restrictions apply.

This article has been accepted for publication in a future issue of this journal, but has not been fully edited. Content may change prior to final publication. Citation information: DOI 10.1109/TIE.2021.3097612, IEEE Transactions on Industrial Electronics

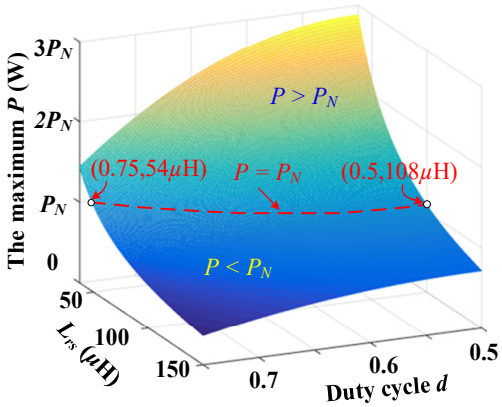

Fig.7. Transmission power versus leakage inductor and duty cycle. ($\varphi = 0.5\pi$, P_N = 1kW).

$$P(L_{rs},d)=\frac{N_s^2V_c^2\left[-8d^2+8d-1\right]T_s}{8N_p^2L_{rs}} \tag{20}$$

Consequently, taking Fig.7 as an example, $L_{rs}\le 54\mu$H should be satisfied to achieve maximum power transfer at the extremely case.

Under rated power P_N, the RMS current of the leakage inductor can be calculated as (21).

L_{eq} is the equivalent inductor, but its physical meaning is uncertain. To deal with this, the study finds that when the TWCI meets certain conditions, it can be completely equivalent to the discrete structure of two DC inductors plus a transformer. The detailed analysis is as follows: it is assumed that the leakage flux through the air is negligible, through the dual transformation method [34], that is, according to the reluctance model of the TWCI shown in Fig.3, the dual transformation is performed to derive the equivalent circuit of the magnet circuit model as shown in Fig.8. And the inductor parameters of the equivalent circuit can be written as

$$L_{dc1}=\frac{N_1^2}{R_1}=\frac{N_p^2}{R_p}=L_{eq},\ L_{dc2}=\frac{N_2^2}{R_2}=\frac{N_p^2}{R_p}=L_{eq} \tag{22}$$

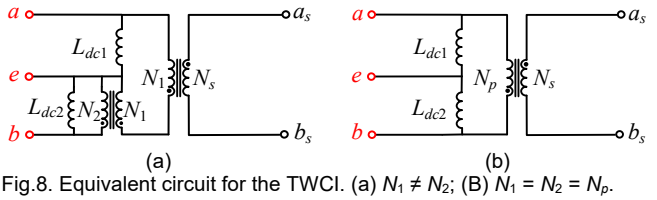

Fig.8. Equivalent circuit for the TWCI. (a) $N_1 \ne N_2$; (B) $N_1 = N_2 = N_p$.

Fig.9 illustrates the curves for the inductor RMS current. Fig. 9(a) illustrates the relationship between the leakage inductor RMS current and the voltage for different leakage inductances. When the leakage inductance L_{rs} is equal to 18μH, the RMS current increases significantly if the voltage is low; when L_{rs} is larger than 50μH, the leakage currents change slightly. As can be seen, the RMS current decreases with the value of leakage inductance increases near V_L = 18 to 33V. However, the trend of leakage inductor RMS current is opposite near V_L = 33 to 36V. That is the RMS current increases with the leakage inductance increases. Considering that more windings will be needed to increase the inductance, the leakage inductance is designed to be 36μH to make a tradeoff between RMS current and copper loss.

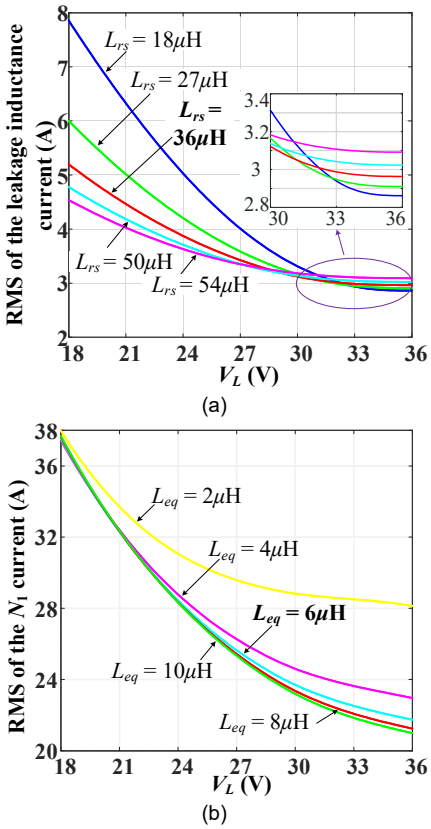

Fig.9. Curves for the RMS current. (a) RMS currents under different values of leakage inductor L_{rs}. (b). RMS currents under different L_{eq} values.

Based the transferred power, the L_{eq} (DC inductor) value is around 10μH when the current ripple is set as 15% of rated average current according to the general engineering design. And when the ripple is 100%, the L_{eq} value is around 2μH. Consequently, Fig.9 (b) illustrates the RMS current curves of the outer-leg windings when L_{eq} changes from 2μH to 10μH. Similar to leakage inductor, considering the magnetic loss of the outer legs and the RMS current, L_{eq} = 6μH is finally selected for the equivalent inductor of the two outer legs.

$$I_{L_{rs}\_RMS}=\begin{cases}\dfrac{V_HT_s}{2\pi L_{rs}}\sqrt{2\phi(1-d)\left[\phi-(2d-1)\pi\right]-\dfrac{\pi^2}{12}(2d-1)^2(4d-5)} & \begin{Bmatrix}V_{L\_\min}\le V_L\le V_{L\_\mathrm{div}}\\ \phi\subset\left[0,(2d-1)\pi\right]\end{Bmatrix}\\ \dfrac{V_HT_s}{\pi L_{rs}}\sqrt{\dfrac{\phi\left[\phi(\pi d-\phi)+3\pi^2d(1-2d)\right]}{6\pi}+\dfrac{\pi^2(2d-1)^2(4d-1)}{16}} & \begin{Bmatrix}V_{L\_\mathrm{div}}\le V_L\le V_{L\_\max}\\ \phi\subset\left[(2d-1)\pi,\pi\right]\end{Bmatrix}\end{cases} \tag{21}$$

0278-0046 (c) 2021 IEEE. Personal use is permitted, but republication/redistribution requires IEEE permission. See http://www.ieee.org/publications_standards/publications/rights/index.html for more information.
Authorized licensed use limited to: Central South University. Downloaded on August 12,2021 at 11:35:38 UTC from IEEE Xplore. Restrictions apply.

This article has been accepted for publication in a future issue of this journal, but has not been fully edited. Content may change prior to final publication. Citation information: DOI 10.1109/TIE.2021.3097612, IEEE Transactions on Industrial Electronics

C、 TWCI Design Considerations

The physical topology of TWCI is shown in Fig.10. The standard EE cores and the Litz wire windings constitute the TWCI structure. According to Fig.8, the two windings on the outer legs function as the equivalent inductors as well as the transformer primary. It can not only reduce the volume of the magnetic element, but also reduce the input current ripple. The winding of the center leg can be used as the transformer secondary winding.

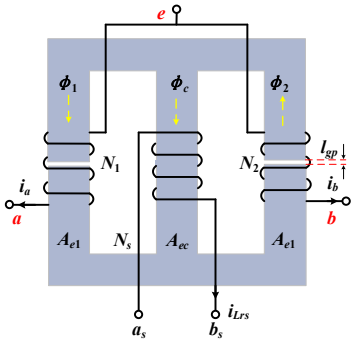

Fig.10. Physical topology of TWCI using EE cores.

Different TWCI structures will produce different inherent leakage inductance. The structure A of TWCI is shown in Fig.11(a). Since the windings are all separated, it will produce a large leakage inductance, and reduce the maximum transmission power of the converter. In order to reduce the leakage inductance, according to source transfer equivalent transformation method, the center leg winding can be split into two outer leg windings, forming the structure B of TWCI, as Fig.11(b) shown.

By the measurement of impedance analyzer, the leakage inductance parameters of structure A and structure B of TWCI are shown in Table I.

It can be seen that the leakage inductance of the TWCI with winding interleaving structure can be effectively reduced. In order to decrease the leakage inductance, the structure B is finally selected for the prototype in this manuscript.

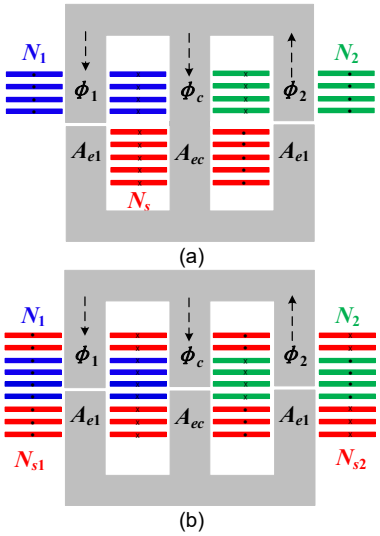

Fig.11. Different structures of TWCI. (a) Structure A of TWCI. (b) Structure B of TWCI.

TABLE Ⅰ.
MEASURED LEAKAGE INDUCTANCE OF DIFFERENT STRUCTURES OF TWCI

Item	leakage inductance
Structure A (μH)	41.6
Structure B (μH)	11.2

Then, the required leakage inductance is obtained by series connection of an external inductor, that is the leakage inductance L_{rs_TWCI} of the TWCI is compensated by an external series inductance L_{rs_series} to realize the required leakage inductance L_{rs}, as Fig.12 shows.

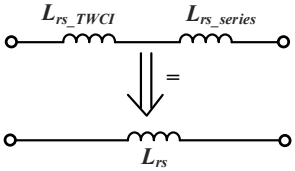

Fig.12. The diagram of external series leakage inductor.

It should be noted that the TWCI central leg does not need the air gap to achieve decoupled-integration of the two outer leg windings. Meanwhile, dc component of the flux is eliminated in the center leg, and the magnetic loss can be eliminated. For the proposed TWCI, parameters including the core reluctance R_p and the numbers of turns of the windings N_p, N_s need to be determined. The detailed design process of TWCI is as follows.

In order to limit the core loss of a specified material, the maximum flux density change of the core is set as 150mT. And then the turns number N_p ($N_1 = N_2 = N_p$) of the two LVS windings of TWCI can be calculated as

$$N_P = \frac{dV_L T_s}{\Delta B A_e} \tag{23}$$

where ΔB is the change of the magnetic flux density, A_e is the cross-sectional area of the two outer legs of EE42 cores, and d is the duty cycle. And according to (15), the turns number N_s of the HVS winding of TWCI can be obtained.

The self-inductances of two outer legs of TWCI are DC equivalent inductances L_{eq}, and $L_{eq} = 6\mu$H has been designed to obtain low RMS current. According to the (22), the air gap reluctances of two outer legs can be derived, and the air gap length of two outer legs can be written as

$$l_{gp} = R_p \mu_0 A_e \tag{24}$$

where μ_0 is space permeability.

According to the magnetic flux expression (1), the magnetic flux waveforms can be obtained, as shown in Fig.13.

And the flux densities in each core leg are estimated as

$$\begin{cases} B_1 = \dfrac{N_p i_a + N_s i_{Lrs}}{R_P A_{e1}} \\ B_c = \dfrac{-N_p (i_a - i_b) - 2N_s i_{Lrs}}{R_P A_{ec}} \\ B_2 = \dfrac{-N_s i_{Lrs} + N_p i_b}{R_P A_{e2}} \end{cases} \tag{25}$$

where A_{e1}, A_{e2} and A_{ec} are cross-sectional areas of the two outer legs and the center post respectively.

0278-0046 (c) 2021 IEEE. Personal use is permitted, but republication/redistribution requires IEEE permission. See http://www.ieee.org/publications_standards/publications/rights/index.html for more information.
Authorized licensed use limited to: Central South University. Downloaded on August 12,2021 at 11:35:38 UTC from IEEE Xplore. Restrictions apply.

This article has been accepted for publication in a future issue of this journal, but has not been fully edited. Content may change prior to final publication. Citation information: DOI 10.1109/TIE.2021.3097612, IEEE Transactions on Industrial Electronics

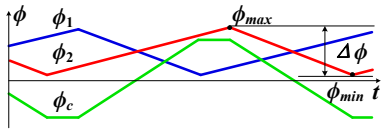

Fig.13. The magnetic flux waveforms of the TWCI.

D、Design and Loss Breakdown Comparison Between TWCI DAB and CF-DAB

Fig.8 (b) describes the structure of discrete magnetic parts with two inductors and a transformer. The parameters for comparisons of TWCI and discrete magnetics are shown in Table II. As previously discussed, $N_1 = N_2$, and $R_1 = R_2$ are adopted for the TWCI. The core type is selected to ensure that the change of magnetic flux density to be the same. The proposed TWCI using a single EE42 can reduce the magnetic core occupied volume and achieve a higher power density compared with the two UF25 boost DC inductors and one EE42 transformer in the CF-DAB.

TABLE Ⅱ.
COMPARISON OF DIFFERENT MAGNETIC PARTS DESIGNS

Magnetic category	discrete magnetics		TWCI DAB
	transformer design	2×inductor design	
Core material	Mn-Zn power ferrite DMR40		
Core model	EE42	UF25	EE42
Length (mm)	42	2×25	42
Width (mm)	20	2×13	20
Height (mm)	42	2×40	42
Magnetic flux density change (T)	ΔB=0.15	B_{max}=0.39 (ΔB=0.158)	ΔB=0.15
Effective *Ve* (mm^3)	22601	2×9264.4	22601
Effective *Ae* (mm^2)	233	106	233
Turns	N_1:N_2=5:25	2×5	N_p:N_s=5:25
Wire diameter (mm)		d = 0.1	
Window factor	0.197	0.15	0.246

The loss breakdown comparisons between the discrete magnetics case of CF-DAB and the proposed TWCI DAB at different V_L (V_L = 18V, 27V and 36V) and different loads (P = 100W and 1000W) are shown in Fig.14. P_{TWCI_DAB} and $P_{CF\text{-}DAB}$ are total losses of TWCI DAB converter and CF-DAB converter, respectively. P_{TWCI_copper} and P_{TWCI_core} are copper loss and core loss of the TWCI DAB converter, respectively. And $P_{TWCI\_Lrs\_copper}$ and $P_{TWCI\_Lrs\_core}$ are copper loss and core loss of the leakage inductor in TWCI DAB converter, respectively. P_{Ldc_copper} and P_{Ldc_core} are copper loss and core loss of the two DC inductors in CF-DAB converter, respectively. P_{T_copper} and P_{T_core} are copper loss and core loss of the transformer in CF-DAB converter, respectively. And P_{Lrs_copper} and P_{Lrs_core} are copper loss and core loss of the leakage inductor in CF-DAB converter, respectively. $P_{turn\text{-}on}$ and $P_{turn\text{-}off}$ are turn-on loss and turn-off loss of all the switches, respectively. And P_{con} is conduction loss for switches. P_{dri} is driving loss. Under the PWM modulation strategy, the driving signals for the two switches in any bridge are complementary. The conduction of the antiparallel diode only exists in the dead time, and it lasts for a very short time. Thus, the conduction loss of antiparallel diode is ignored in this paper to simplify the analysis. Except for the difference of two DC inductors and transformers, other experimental parameters are the same, such as MOSFETs, PCB circuit boards, etc. In TWCI DAB, all the MOSFETs are turned on with ZVS. Hence, the turn-on losses are zero. The total losses consist of four parts, namely driving loss, switches loss, external inductor loss, and TWCI loss. As Fig.14(a) shown, when the converter works at V_L = 18V and light load (100W), the total loss of CF-DAB is higher than that of the proposed TWCI DAB about 6W, which is mainly caused by hard turning off loss, leading to low efficiency at light load. When V_L = 36V, the difference is reduced to 3W. As the input voltage increases, the current decreases, then the turn-off loss and the copper loss of the magnetic elements decrease. As Fig.14(b) shown, when the converter works at V_L = 18V and heavy load condition (1000W), the power loss with the proposed CF-DAB is higher than that of TWCI DAB about 6.6W, which is mainly caused by the increased core and copper losses. Based on the theory of Steinmetz Equation [35], the product of the magnetic loss density of each leg and the effective volume is used to obtain the magnetic core loss of TWCI.

At low input voltages condition, the conduction time and input current increases as the input voltage decreases. The corresponding switching loss and magnetic element loss increase. Magnetic element loss and hard turn off loss dominate

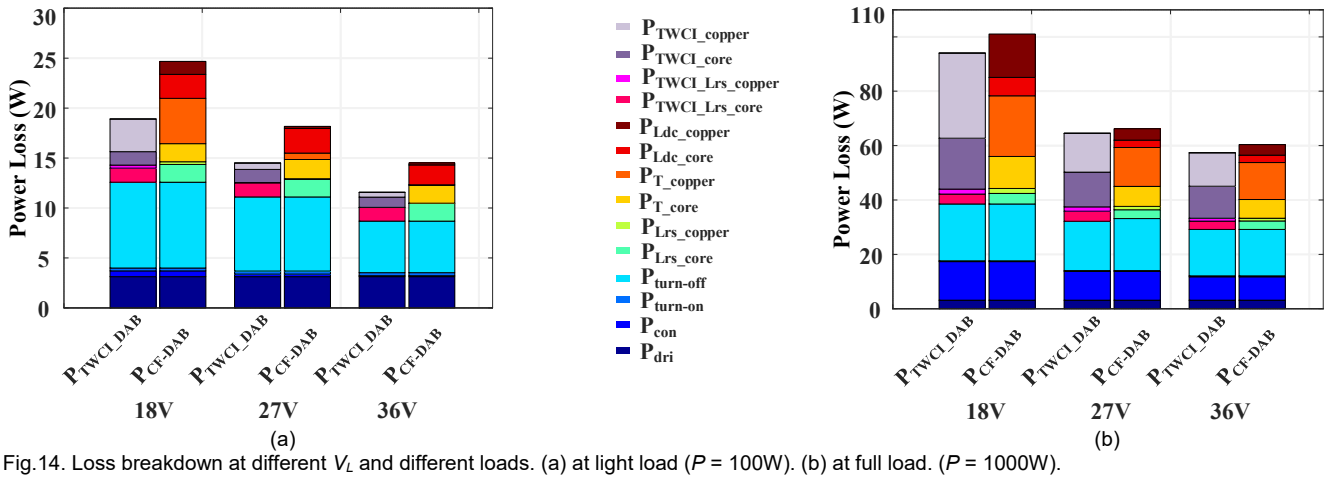

Fig.14. Loss breakdown at different V_L and different loads. (a) at light load (P = 100W). (b) at full load. (P = 1000W).

0278-0046 (c) 2021 IEEE. Personal use is permitted, but republication/redistribution requires IEEE permission. See http://www.ieee.org/publications_standards/publications/rights/index.html for more information.
Authorized licensed use limited to: Central South University. Downloaded on August 12,2021 at 11:35:38 UTC from IEEE Xplore. Restrictions apply.

This article has been accepted for publication in a future issue of this journal, but has not been fully edited. Content may change prior to final publication. Citation information: DOI 10.1109/TIE.2021.3097612, IEEE Transactions on Industrial Electronics

at light loads, leading to low efficiency at light load. As can be seen, the total loss of the integrated magnetic TWCI is reduced according to Fig.14. Therefore, TWCI DAB efficiency is higher than CF-DAB.

In addition to the benefits of easy to manufacture and leakage inductance reduction, the proposed TWCI can be modeled and analyzed directly with combination of the magnetic circuit and the electrical circuit, which can simplify the analysis process compared with analyzing them separately. On this basis, a general analysis method of TWCI is provided. In addition, according to Table II, when transmitting the same power, the power density of TWCI DAB can also be increased due to the reduction of core number and volume. Furthermore, efficiency of TWCI DAB is higher than CF-DAB with discrete magnetics according to the loss breakdown.

V. SUBMISSION OF FINAL MANUSCRIPT

In order to verify the effectiveness of the design method, a 1kW experimental prototype is built. And the experimental prototype is shown in Fig.15. The system specifications are illustrated in TABLE III. All the design parameters are designed taking into consideration the safe operation of converter for highest LVS current, i.e.,18V LVS voltage and 1kW output power.

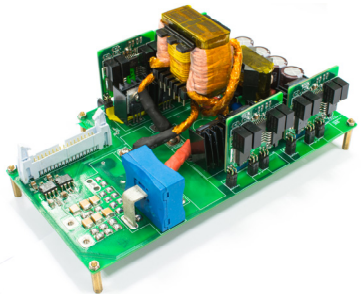

Fig.15. The experimental prototype.

TABLE Ⅲ.
SYSTEM SPECIFICATIONS

P	1kW	L_{rs}	36μH
f	150kHz	L_{eq}	6μH
V_L	18~36V	n	5
V_H	360V	C_c	60μF
Q_1,Q_2,Q_{1a},Q_{2a}	IPP023N10N5	S_1-S_4	UJ3C065030K3S

A、 Equivalent Inductance L_{eq} Design

In practice, the first consideration of the equivalent inductance L_{eq} is the ZVS performance of the LVS switches. According to Fig.6 (a), (b), (c) and (d), the appropriate value range [2μH, 10μH] of L_{eq} can be preliminarily selected. On the other hand, the RMS current should be discussed based on the allowed current ripple to obtain the optimized inductance L_{eq}. Taking the ZVS design of the LVS switches, current ripple and RMS current into consideration, L_{eq} is designed to be 6μH.

B、 Turns Ratio of TWCI Design

The turns ratio of TWCI should be designed to ensure the voltage matching control, that is the voltage of clamping capacitor V_{Cc} matches the output voltage V_H. The clamping voltage V_{Cc} = 72V and the output voltage V_H = 360V. According to (15), the turns ratio of TWCI is $n = N_s/N_p = V_H/V_{Cc} = 5$.

C、 Leakage Inductance L_{rs} Design

The ZVS performance of the HVS switches is affected by the value of the leakage inductance L_{rs}. According to Fig.6 (e) and (f), the appropriate value range [18μH, 54μH] of L_{rs} can be preliminarily selected. In addition, the leakage inductor is closely related to the output power. Thus, $L_{rs} \le 54\mu$H should be satisfied to achieve maximum power transfer form Fig.7. Besides, the optimized leakage inductor is designed by the tradeoff between RMS current and copper loss based on the analysis of RMS current from Fig.9 (a). Based on considering the ZVS range, maximum power transfer capability and the RMS current, the leakage inductance L_{rs} = 36μH is finally selected.

D、 Clamping Capacitor Selection

The selection of the clamping capacitor C_c should ensure that the voltage ripple across C_c is confined within an allowed range. Due to the complementary of the LVS modulation, only half a switching cycle [t_0, t_6) is analyzed. The clamping voltage $v_{Cc}(t)$ can be calculated by

$$v_{Cc}(t) = \frac{1}{C_c}\int_{t_3}^{t} i_a(t)dt + v_{Cc}(t_3) \tag{26}$$

The current i_a will charge/discharge Cc. During [t_3, t_4), i_a is larger than zero, so Cc will be charged and v_{Cc} will rise; while during (t_4, t_6), i_a is smaller than zero, so Cc is discharged and v_{Cc} will fall. So, the maximum of v_{Cc} is at t_4, and minimum one is either at t_3 or t_6. So the voltage ripple ΔV_{Cc} across Cc can be illustrated as

$$\Delta V_{Cc} = v_{Cc}(t_4) - \min\{v_{Cc}(t_3), v_{Cc}(t_6)\} \tag{27}$$

ΔV_{Cc} is designed to satisfy the following criteria:

$$\Delta V_{Cc} / V_{Cc} \le 1\% \tag{28}$$

Calculation for the case of 18V input and 1kW load, the critical value for Cc can be obtained

$$C_c \ge 42.3\,\mu\text{F} \tag{29}$$

A near 40% margin is designed. Thus, the clamping capacitor is selected to be 60μF.

E、 Switches Selection

Considering the maximum voltage across the LVS switches $V_{Q1\_Q1a\_Q2\_Q2a}$ is the clamping voltage V_{Cc}, that is $V_{Q1\_Q1a\_Q2\_Q2a}$ = 72V. And the maximum voltage across the HVS switches $V_{S1\_S2\_S3\_S4}$ is the output voltage V_H, that is $V_{S1\_S2\_S3\_S4}$ = 360V. The current stresses of LVS switches $I_{Q1} = i_a(t_1) = 60.67$A. And the current stresses of HVS switches $I_{S1} = i_{Lrs}(t_5) = 10.71$A. According to the voltage, current stresses and margin should be considered, device type IPP023N10N5 from Infineon company is selected for the LVS switches, and device type UJ3C065030K3S from United SiC company is selected for the HVS switches.

0278-0046 (c) 2021 IEEE. Personal use is permitted, but republication/redistribution requires IEEE permission. See http://www.ieee.org/publications_standards/publications/rights/index.html for more information.
Authorized licensed use limited to: Central South University. Downloaded on August 12,2021 at 11:35:38 UTC from IEEE Xplore. Restrictions apply.

This article has been accepted for publication in a future issue of this journal, but has not been fully edited. Content may change prior to final publication. Citation information: DOI 10.1109/TIE.2021.3097612, IEEE Transactions on Industrial Electronics

VI. Experimental Results

Fig.16 shows the steady-state waveforms of the proposed TWCI DAB in boost mode under different voltages and loads. As shown, v_{ab}, v_{cd}, V_H, i_{Lrs} are the voltages and current of the proposed TWCI DAB, as described in Fig.1. Fig.16 (a) - (c) describe the steady-state waveforms at light load with V_L = 18, 27, 36V, respectively. The corresponding duty cycle of Fig.16 (a) - (c) is d = 0.75, = 0.625, and = 0.5, respectively. It is seen that the pulse width of the midpoint voltage v_{cd} between the HVS bridges is always fixed at 0.5 in these figures, which means the duty cycle of HVS switches is always equal to 0.5. The waveforms of the LVS voltage v_{ab} are similar when d > 0.5. When d = 0.5, the operation waveforms of the PPS control is exactly the same as a SPS controlled converter. In addition, v_{cd} lags behind v_{ab} in phase to adjust the power among all waveforms. Meanwhile, the current slope is zero when both v_{ab} and v_{cd} have been regulated to be stabilized values with the same polarity. Similarly, Fig.16 (d) - (f) and (g) - (i) depict steady-state waveforms at half load and full load, respectively. These demonstrate the working principle of the proposed TWCI DAB. And it is clear that the experimental waveforms coincide with the theoretical analysis pretty well.

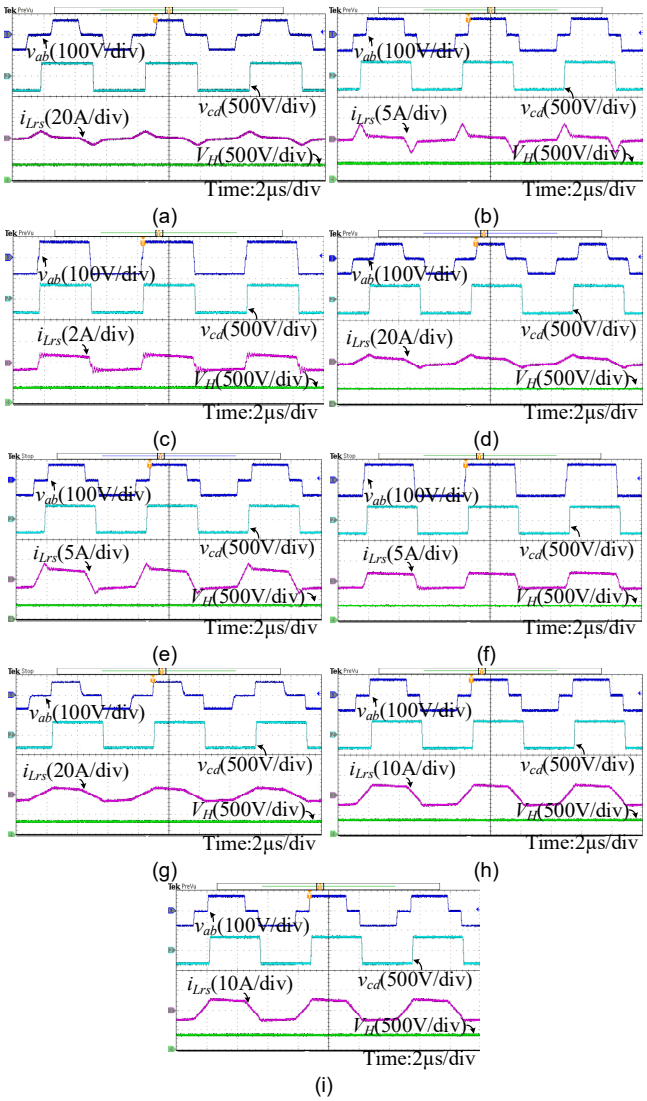

Fig.16. Steady-state waveforms with the proposed TWCI DAB. (a) at light load when V_L =18V. (b) at light load when V_L =27V. (c) at light load when V_L =36V. (d) at half load when V_L =18V. (e) at half load when V_L =27V. (f) at half load when V_L =36V. (g) at full load when V_L =18V. (h) at full load when V_L =27V. (i) at full load when V_L =36V.

The ZVS experimental waveforms of switches are shown in Fig.17 and Fig.18. Compared to heavy load, it is most difficult to achieve ZVS under light load. Meanwhile, compared with the top switch Q_{1a} of LVS and the bottom switch Q_2 of LVS, S_1

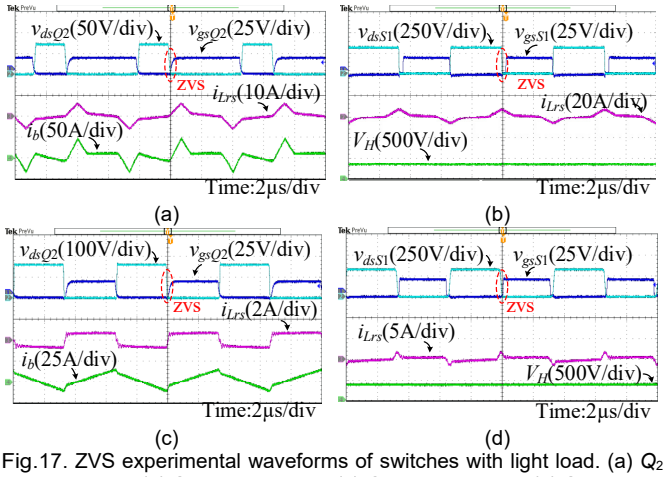

Fig.17. ZVS experimental waveforms of switches with light load. (a) Q_2 when V_L =18V. (b) S_1 when V_L =18V. (c) Q_2 when V_L =36V. (d) S_1 when V_L =36V.

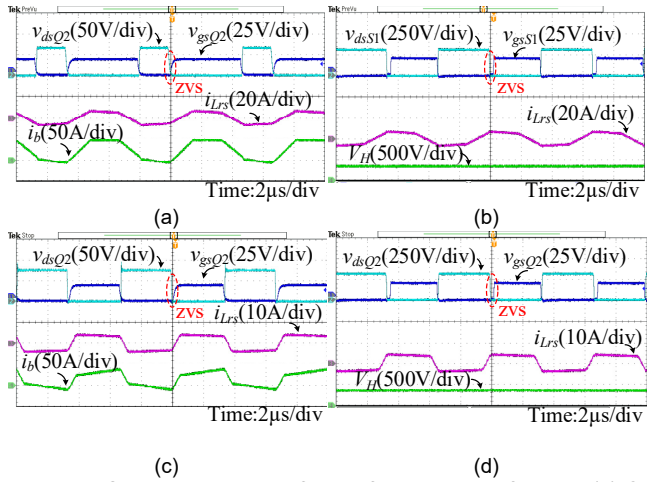

Fig.18. ZVS experimental waveforms of switches with full load. (a) Q_2 when V_L =18V. (b) S_1 when V_L =18V. (c) Q_2 when V_L =36V. (d) S_1 when V_L =36V.

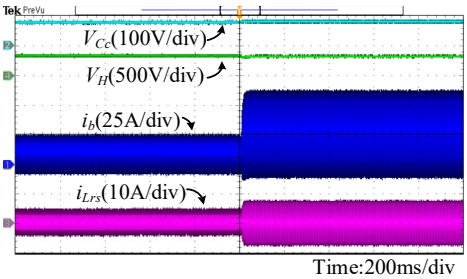

Fig.19. Load-step experimental result from half load to full load with V_L =27V.

0278-0046 (c) 2021 IEEE. Personal use is permitted, but republication/redistribution requires IEEE permission. See http://www.ieee.org/publications_standards/publications/rights/index.html for more information.
Authorized licensed use limited to: Central South University. Downloaded on August 12,2021 at 11:35:38 UTC from IEEE Xplore. Restrictions apply.

This article has been accepted for publication in a future issue of this journal, but has not been fully edited. Content may change prior to final publication. Citation information: DOI 10.1109/TIE.2021.3097612, IEEE Transactions on Industrial Electronics

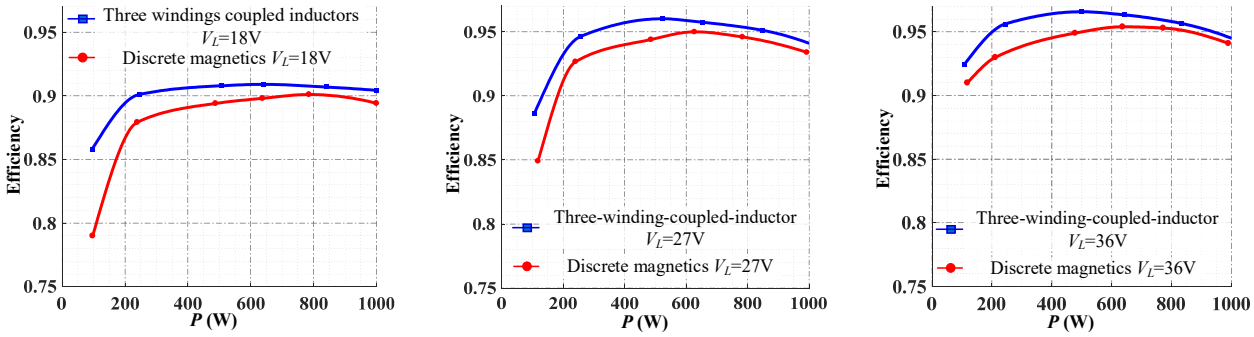

(a) (b) (c)

Fig.20. Efficiency comparisons between the proposed TWCI DAB and CF-DAB at different loads and different voltages. (a) V_L=18V. (b) V_L=27V. (c) V_L=36V.

of HVS are more difficult to realize ZVS. Consequently, Fig.17 illustrates the ZVS experimental waveforms of the bottom switch Q_2 of LVS and switch S_1 of HVS under different voltages at light load. The results show that ZVS can be achieved despite the voltage fluctuations at light load.

Fig.18 illustrates the ZVS experimental waveforms of the bottom switch Q_2 of LVS and S_1 of HVS at different voltages at full load. It can be seen that ZVS can be achieved when input voltage changes.

Fig.19 illustrates the load-step experimental result from half load to full load with V_L=27V. V_H can keep stable and can return to the steady state value within 20ms.

Fig.20 shows the measured efficiency at different loads and different voltages. In order to verify the effectiveness of the TWCI DAB, the discrete magnetic case of CF-DAB is also measured. The overall conversion efficiency is high, and the highest efficiency of the TWCI DAB reaches 95.7%. The proposed TWCI DAB achieves higher efficiency than the discrete magnetic elements of CF-DAB with the same magnetic material. The power loss at light load can be reduced for TWCI DAB, because the core loss makes up the majority of the total loss when converter operates at light load condition.

VII. Conclusions

In this paper, a TWCI DAB converter is proposed. Similar to the CF-DAB, the proposed TWCI DAB can achieve small input current ripple and wide input voltage range. In addition, the integrated magnetic structure can make the converter more efficient and improve the power density significantly. With the adopted PWM modulation, the proposed TWCI DAB can achieve ZVS of the primary and secondary side switches within the full load range under wide voltage range. In addition, the design of equivalent inductor L_{eq} and leakage inductor are introduced considering the maximum power transmission, soft switching conditions and RMS current. The experimental results of the proposed prototype verified the effectiveness of the proposed solution.

References

[1] H. Qian, J. Zhang, J.-S. Lai, and W. Yu, "A high-efficiency grid-tie battery energy storage system," *IEEE Trans. Power Electron.*, vol. 26, no. 3, pp. 886–896, Mar. 2011.

[2] G.-J. Su and L. Tang, "A reduced-part, triple-voltage DC–DC converter for EV/HEV power management," *IEEE Trans. Power Electron.*, vol. 24, no. 10, pp. 2406–2410, Oct. 2009.

[3] S. T. Sushil, G. W. Rupesh, and A. Vivek, "A novel reconfigurable microgrid architecture with renewable energy sources and storage," *IEEE Trans. on Ind. Applicat.*, vol. 51, no. 2, pp. 1805–1816, Mar. 2015.

[4] E. Michael, M. M. U. Rehman, H. Kelly, Z. Regan, C. Daniel, and M. Dragan, "Active balancing system for electric vehicles with incorporated low-voltage bus," *IEEE Trans. Power Electron.*, vol. 31, no. 11, pp. 7887–7895, Nov. 2016.

[5] Y.-W. Cho, W.-J. Cha, J.-M. Kwon, and B.-H. Kwon, "High-efficiency bidirectional DAB inverter using a novel hybrid modulation for stand-alone power generating system with low input voltage," *IEEE Trans. Power Electron.*, vol. 31, no. 6, pp. 4138–4147, Jun. 2016.

[6] B. Zhao, Q. Yu, and W. Sun, "Extended-phase-shift control of isolated bidirectional DC–DC converter for power distribution in microgrid," *IEEE Trans. Power Electron.*, vol. 27, no. 11, pp. 4667–4680, Nov. 2012.

[7] B. Zhao, Q. Song, W. Liu, and W. Sun, "Current-stress-optimized switching strategy of isolated bidirectional DC–DC converter with dual-phase-shift control," *IEEE Trans. Ind. Electron.*, vol. 60, no. 10, pp. 4458–4467, Oct. 2013.

[8] G. Xu, D. Sha, Y. Xu, and X. Liao, "Hybrid-bridge-based DAB converter with voltage match control for wide voltage conversion gain application," *IEEE Trans. Power Electron.*, vol. 33, no. 2, pp. 1378–1388, Feb. 2018.

[9] Y. Shen, X. Sun, W. Li, X. Wu, and B. Wang, "A modified dual active bridge converter with hybrid phase-shift control for wide input voltage range," *IEEE Trans. Power Electron*., vol. 31, no. 10, pp. 6884–6900, Oct. 2016.

[10] G. Xu, L. Li, X. Chen, Y. Liu, Y. Sun, and M. Su, "Optimized EPS control to achieve full load range ZVS with seamless transition for dual active bridge converters," *IEEE Trans. Ind. Electron, Early Access Article*, 2020, DOI: 10.1109/TIE.2020.3014562.

[11] Y. Hyunjae, S. Seung-Ki, P. Yongho, and J. Jongchan, "System integration and power-flow management for a series hybrid electric vehicle using supercapacitors and batteries," *IEEE Trans. on Ind. Applicat.*, vol. 44, no. 1, pp. 108–114, 2008.

[12] D. Sha, J. Zhang, X. Wang, and W. Yuan, "Dynamic response improvements of parallel-connected bidirectional DC–DC converters for electrical drive powered by low-voltage battery employing optimized feedforward control," *IEEE Trans. Power Electron.*, vol. 32, no. 10, pp. 7783–7794, Oct. 2017.

[13] F. Z. Peng, H. Li, G.-J. Su, and J. S. Lawler, "A new ZVS bidirectional DC–DC converter for fuel cell and battery application," *IEEE Trans. Power Electron.*, vol. 19, no. 1, pp. 54–65, Jan. 2004.

[14] H.-J. Chiu and L.-W. Lin, "A bidirectional DC–DC converter for fuel cell electric vehicle driving system," *IEEE Trans. Power Electron.*, vol. 21, no. 4, pp. 950–958, Jul. 2006.

[15] J. Zhang, H. Wu, X. Qin, and Y. Xing, "PWM plus secondary-side

0278-0046 (c) 2021 IEEE. Personal use is permitted, but republication/redistribution requires IEEE permission. See http://www.ieee.org/publications_standards/publications/rights/index.html for more information.
Authorized licensed use limited to: Central South University. Downloaded on August 12,2021 at 11:35:38 UTC from IEEE Xplore. Restrictions apply.

This article has been accepted for publication in a future issue of this journal, but has not been fully edited. Content may change prior to final publication. Citation information: DOI 10.1109/TIE.2021.3097612, IEEE Transactions on Industrial Electronics

phase-shift controlled soft-switching full-bridge three-port converter for renewable power systems," *IEEE Trans. Ind. Electron.*, vol. 62, no. 11, pp. 7061–7072, Nov. 2015.

[16] X. Pan and K. R. Akshay, "Novel bidirectional snubberless naturally commutated soft-switching current-fed full-bridge isolated DC/DC converter for fuel cell vehicles," *IEEE Trans. Ind. Electron.*, vol. 61, no. 5, pp. 2307–2315, May. 2014.

[17] H. Xiao and S. Xie, "A ZVS bidirectional DC–DC converter with phase-shift plus PWM control scheme," *IEEE Trans. Power Electron.*, vol. 23, no. 2, pp. 813–823, Mar. 2008.

[18] D. Sha, Q. Lin, F. You, X. Wang, and G. Xu, "A ZVS bidirectional three-level DC–DC converter with direct current slew rate control of leakage inductance current," *IEEE Trans. on Ind. Applicat.*, vol. 52, no. 3, pp. 2368–2377, May. 2016.

[19] D. Sha, J. Zhang, and K. Liu, "Leakage inductor current peak optimization for dual-transformer current-fed dual active bridge DC-DC converter with wide input and output voltage range," *IEEE Trans. Power Electron.*, vol. 35, no. 6, pp. 6012–6024, Jun. 2020.

[20] D. Sha, X. Wang, K. Liu, and C. Chen, "A current-fed dual-active-bridge DC–DC converter using extended duty cycle control and magnetic-integrated inductors with optimized voltage mismatching control," *IEEE Trans. Power Electron*., vol. 34, no. 1, pp. 462–473, Jan. 2019.

[21] C. Jiang, and H. Liu, "A Novel Interleaved Parallel Bidirectional Dual-Active-Bridge DC–DC Converter with Coupled Inductor for More-Electric Aircraft," *IEEE Trans. Ind. Electron.*, vol. 68, no. 2, pp. 1759–1768, Feb. 2021.

[22] H. Bahrami, S. Farhangi, H. Iman-Eini, and E. Adib, "A New Interleaved Coupled-Inductor Nonisolated Soft-Switching Bidirectional DC–DC Converter with High Voltage Gain Ratio," *IEEE Trans. Ind. Electron.*, vol. 65, no. 7, pp. 5529–5538, Jul. 2018.

[23] H. Bahrami, S. Farhangi, H. Iman-Eini, and E. Adib, "Analysis, Design, and Implementation of DC–DC IBBC-DAHB Converter with Voltage Matching to Improve Efficiency," *IEEE Trans. Ind. Electron.*, vol. 66, no. 7, pp. 5209–5219, Jul. 2019.

[24] Z. Yan, J. Zeng, W. Lin, and J. Liu, "A Novel Interleaved Nonisolated Bidirectional DC–DC Converter with High Voltage-Gain and Full-Range ZVS," *IEEE Trans. Power Electron.*, vol. 35, no. 7, pp. 7191–7203, Jul. 2020.

[25] J. Liu, Z. Zheng, C. Li, K. Wang, and Y. Li, "Automatic Current Sharing of Input-Parallel Output-Parallel Dual Active Bridge Converters with Coupled Inductors." *2019 IEEE 13th International Conference on Power Electronics and Drive Systems (PEDS)*, pp. 1-6, Feb. 2019.

[26] J. Liu, C. Li, Z. Zheng, K. Wang, Y. Li, "Current Discrepancy Mitigation of Input-Parallel Output-Parallel Dual Active Bridge Converters Using Coupled Inductors," *IEEE Trans. Ind. Electron.*, Early Access Article, 2020, DOI: 10.1109/TIE.2020.3013793.

[27] Z. Guo, D. Sha, "Dual-Active-Bridge Converter with Parallel-Connected Full Bridges in Low-Voltage Side for ZVS by Using Auxiliary Coupling Inductor," *IEEE Trans. Ind. Electron.*, vol. 66, no. 9, pp. 6856–6866, Sep. 2019.

[28] N. Mostafa *et al., "*A current sharing method utilizing single balancing transformer for a multiphase LLC resonant converter with integrated magnetics," *IEEE J. Emerg. Sel. Topics Power Electron.*, vol. 6, no. 2, pp. 977–992, 2018.

[29] Y.-T. Chen, Z.-M. Li, and R.-H. Liang, "A novel soft-switching interleaved coupled-inductor boost converter with only single auxiliary circuit," *IEEE Trans. Power Electron.*, vol. 33, no. 3, pp. 2267–2281, 2018.

[30] H. Wu, K. Sun, L. Chen, L. Zhu, and Y. Xing, "High step-up/step-down soft-switching bidirectional DC–DC converter with coupled-inductor and voltage matching control for energy storage systems," *IEEE Trans. Ind. Electron.*, vol. 63, no. 5, pp. 2892–2903, 2016.

[31] Y. Yang, J. Ma, C. N.-M. Ho, and Y. Zou, "A new coupled-inductor structure for interleaving bidirectional DC-DC converters," *IEEE J. Emerg. Sel. Topics Power Electron.*, vol. 3, no. 3, pp. 841–849, 2015.

[32] C. Peng, M. Hannigan, and O. Seiersen, "A new efficient high frequency rectifier circuit," *High Frequency Power Conversion (HFPC'91) Conference*, pp. 236–243, 1991.

[33] W. Chen, G. Hua, S. Dan, and F. Lee, "Design of high efficiency, low profile, low voltage converter with integrated magnetics," *Applied Power Electronics Conference*, pp. 911–917, Feb. 1997.

[34] Bloom and Gordon, Modern DC-to-DC switchmode power converter circuits. Van Nostrand Reinhold Inc, pp. 262-325, 1985.

[35] M. H. Ahmed, C. Fei, F. Lee, and Q. Li "Single-Stage High-Efficiency 48/1 V Sigma Converter with Integrated Magnetics," *IEEE Trans. Ind. Electron.*, vol. 67, no. 1, pp. 192–202, Jan. 2020.

Hua Han received the M.S. and Ph.D. degrees fromthe School of Automation, Central South University,Changsha, China, in 1998 and 2008, respectively.She was a Visiting Scholar with the University ofCentral Florida, Orlando, FL, USA, from 2011 to2012. She is currently a Professor with the Schoolof Automation, Central South University.

Her research interests include microgrids, renew-able energy power generation systems, and powerelectronic equipment.

Jing Guo was born in Shaanxi, China, in 1997. He received the B.S. degree in electrical engineering and automation from Zhejiang Sci-Tech University, Hangzhou, China, in 2019, currently pursuing the M.S. degree in electrical engineering at Central South University, Changsha, China.

His research interests include magnetic integration design and soft switching technology for bidirectional DC-DC converters.

Guo Xu (M'15) received the B.S. degree in electrical engineering and automation and the Ph.D. degree from the Beijing Institute of Technology, Beijing, China, in 2012 and 2018, respectively. From 2016 to 2017, he was a Visiting Student with the Center for Power Electronics System, Virginia Polytechnic Institute and State University, Blacksburg, VA, USA. Since 2018, he has been with the School of Automation, Central South University, Changsha, China, where he is currently an Associate Professor.

His research interests include modeling and control of power electronics converters, high-efficiency power conversion, and magnetic integration in power converters.

Jingtao Xu was born in Hubei, China, in 1994. He received the B.S. and M.S. degree in electrical engineering and automation from Central South University, Changsha, China, in 2016 and 2019. He is currently working toward the Ph.D. degree in electrical engineering.

His research interests include modeling and control of power electronics converters.

Dong Liu (Senior Member, IEEE) received the B.Eng. and M.Sc. in electrical engineering from South China University of Technology, Guangzhou, China, in 2008 and 2011, and the Ph.D. degree in energy technology from the Department of Energy Technology, Aalborg University, Aalborg, Denmark, in 2018. From

0278-0046 (c) 2021 IEEE. Personal use is permitted, but republication/redistribution requires IEEE permission. See http://www.ieee.org/publications_standards/publications/rights/index.html for more information.
Authorized licensed use limited to: Central South University. Downloaded on August 12,2021 at 11:35:38 UTC from IEEE Xplore. Restrictions apply.

This article has been accepted for publication in a future issue of this journal, but has not been fully edited. Content may change prior to final publication. Citation information: DOI 10.1109/TIE.2021.3097612, IEEE Transactions on Industrial Electronics

2018 to 2021, he was a Post-Doctoral Researcher in the Department of Energy Technology at the Aalborg University. Currently, he is with the Department of Electronic and Electrical Engineering at the University of Sheffield as a Research Associate. From 2011 to 2014, he was an R&D engineer in Emerson Network Power Co., Ltd., Shenzhen, China. From May 2017 to November 2017, he was a visiting scholar at the Center for Power Electronics Systems (CPES), Virginia Tech, Blacksburg, VA, USA.

His main research interests include the modeling and control of power electronics converters, high-efficiency power conversion systems, and power electronics applications in renewable energy power generations.

Mei Su was born in Hunan, China, in 1967. She received the B.S., M.S. and Ph.D. degrees from the School of Automation, Central South University, Changsha, China, in 1989, 1992 and 2005, respectively. Since 2006, she has been a School of Automation Central South University.

Her research interests include matrix converter, adjustable speed drives, and wind energy conversion system.

0278-0046 (c) 2021 IEEE. Personal use is permitted, but republication/redistribution requires IEEE permission. See http://www.ieee.org/publications_standards/publications/rights/index.html for more information.
Authorized licensed use limited to: Central South University. Downloaded on August 12,2021 at 11:35:38 UTC from IEEE Xplore. Restrictions apply.